Modeling and short circuit detection of 18650 Li-ion cells under mechanical abuse conditions

Elham Sahraei [a,1], John Campbell [b], Tomasz Wierzbicki [c,*]

[a] Impact and Crashworthiness Lab, Massachusetts Institute of Technology, 77 Massachusetts Ave, Room 5-218B, Cambridge, MA 02139, United States
[b] Impact and Crashworthiness Lab, Massachusetts Institute of Technology, 77 Massachusetts Ave, Room 5-218, Cambridge, MA 02139, United States
[c] Impact and Crashworthiness Lab, Massachusetts Institute of Technology, 77 Massachusetts Ave, Room 5-218A, Cambridge, MA 02139, United States

HIGHLIGHTS

► A comprehensive set of mechanical abuse tests were performed on 18650 cylindrical cells.
► Force, displacement, voltage and temperature were measured; onset of short-circuit was detected.
► At short-circuit, a local drop in force was coincident with drop in voltage and rise in temperature.
► A computational model was developed, and short circuit was predicted by a local peak in the force.
► A very good correlation was obtained between the simulation and the test results.

ARTICLE INFO

ABSTRACT

In this research a simple, yet accurate model of a single cell, needed for safety assessment of batteries under mechanical abuse conditions, was developed. Extensive testing was performed on a 18650 lithium ion cell, including indentation by a hemispherical punch, lateral indentation by a cylindrical rod, compression between two flat plates, and three-point bending. The batteries were tested in an environmental chamber at a 10% SOC. A finite element model was developed, composed of shell elements representing outside casing, and solid elements for the active material with a binder lumped together with the current collectors and the separator. The jelly roll is modeled as a homogenized and isotropic material. The homogenous model assumes different properties in tension and compression, but does not account for the effect of structural anisotropy caused by the layered nature of the jelly roll. Very good correlation was obtained between LS Dyna numerical simulation and test results in terms of load −displacement relations, deformed shape of the battery, and initiation and propagation of a crack in the shell casing. The FE model was also capable of predicting the onset of short circuit of the cell.

1. Introduction

Battery packs for Hybrids, Plug-in Hybrids, and Electric Vehicles are assembled from a system of modules with a tight sheet metal casing around them. Each module consists of an array of individual cells which vary in the composition of electrodes and separators from one manufacturer to another. The present paper deals with the development of a procedure for model identification of a cylindrical battery cell subjected to mechanical loading. The model of a battery cell, will serve as a building block for development of a battery pack model in our future research. Crash safety of lithium-ion batteries is an issue frequently discussed, but rarely published in the open forum. There are three interrelated aspects of battery safety: electrical integrity, thermal integrity, and mechanical integrity. The latter was subject of this study. It is important to understand the limits of mechanical integrity, which is indispensable for electric integrity in any vehicle crash to guard against electric short circuit. A lesson learned from published crash tests of an electric car was that a relatively small intrusion to a battery pack has eventually led to a catastrophic event [1].

A typical test on thermal integrity of the cell is intrusion by a nail [2–4]. In many cases, the short circuit resulted in a violent event of sparks, smoke, and explosions. Methods to prevent thermal runaway in new generation of cells are a topic well studied in the

* Corresponding author. Tel.: +1 617 253 2104; fax: +1 617 253 8689.
  E-mail addresses: elhams@mit.edu (E. Sahraei), soupman@mit.edu (J. Campbell), wierz@mit.edu (T. Wierzbicki).
[1] Tel.: +1 617 324 5025.

Nomenclature

σ_0	average flow stress of shell casing
ϵ_f	fracture strain of shell casing
δ	depth of indentation
l	distance between two supports
t	thickness of shell casing
F	force
R	radius of the battery
σ	stress
ϵ	strain
σ_{TC}	tensile cut off value
σ_θ	hoop stress
p	pressure
μ	friction coefficient
E	Young modulus
L	length of the battery

battery community [5,6]. Most of the articles report on advances on electrochemistry, and it is difficult to find a paper on mechanical properties of the jelly roll undergoing large deformations, as could be seen in a vehicle crash. The investigators are aware that there have been several efforts to model mechanical behavior of batteries in the elastic range [7–9]. However, elastic analysis would not give any clues about failure of internal and external components of battery cells, including failure of the separator leading to short circuit. In this paper, a general procedure will be outlined on the development of a constitutive and computational model of an 18650 cylindrical cell. It will be shown that an average homogenized property of a battery cell combined with a constitutive model of high density foam can be determined through a combination of physical testing and closed form solutions. In order to predict the strength and deformation of the battery cell in different load scenarios, a suitable constitutive model of the jelly roll is required. There are two possible approaches to develop such a model. One is to consider the jelly roll as a laminated composite, and estimate the material properties based on the properties of a system of individual layers of active electrodes, electrode collectors, and the separator. This approach will be pursued in the course of the new MIT consortium on modeling and safety of lithium ion batteries. The other method is to consider the jelly roll as a homogenized material and estimate the properties based on physical testing on the whole cell [10–12]. The second method is adopted for this study, as it is considerably more time-efficient in terms of model development and FE simulation time. It also gives a reasonably accurate prediction of the behavior of the cell, including the determination of the point of short circuit.

The main objective is to predict force displacement and energy absorption of cells under local deformation of battery due to mechanical loading. This study uses extensive testing of the battery cell and jelly roll of a commercially available 18650 lithium-ion cylindrical cell. Then, finite element model of the cell was developed, calibrated, and validated against several loading cases. The model provides information on the history of stress and strain in the representative volume element.

The second objective is to develop criteria to detect onset of short-circuit under mechanical loads. In the present paper, a procedure will be presented to predict onset of electric short-circuit using a homogenized model. For that purpose, the properties of all layers are lumped together into a single material model. In order to detect the series of events leading to short-circuit in the cell, a detailed model of the layered structure of the jelly-roll is under development.

It should be pointed out that the electric short-circuit is a necessary, but not sufficient condition for the occurrence of thermal runaway in the case of mechanical abuse. Chemistry of the cell, resistance of separator to heat, size of the fractured part, and rate of heat transfer all play a role in processes leading to a thermal runaway. If the cell has not gone to thermal runaway right away, it can still go into a slow process of electrochemical reaction, releasing gases that eventually could lead to a catastrophic event. Therefore, the authors believe that the task of predicting electric short-circuit is of important contribution to the battery community.

2. Test program on 18650 cylindrical cells

The most common commercially available lithium-ion cell is the 18650 cell which offers many testing advantages. The cell is approximately 18 mm in diameter and 65 mm in length. Its small size allows the use of most standard load–displacement testing machines with minimal cleanup after any electrolyte leakage, even when testing the cells with endcaps removed. Testing many of these is not nearly as expensive as the larger cells which may only be tested a few times due to the larger cost involved per cell. The steel shell casing of the 18650 protects and adds axial and lateral strength to the cell. Furthermore, the size and shape of these cells allows many cells to be combined into one battery pack. For the present study that is aimed at developing general testing and modeling procedures, the choice of a particular manufacturer is unimportant. Commercially available 18650 cylindrical lithium-ion batteries with lithium cobalt dioxide chemistry were purchased. The specifications of the batteries used for this study are detailed in Table 1. The cells were 50% discharged when shipped by manufacturers.

2.1. Mechanical testing of shell casing

The plastic properties of the shell casing were not obtained from the manufacturer, but rather, determined from our own tests. The manufacturing process consists of deep drawing of cans from rolled steel sheets. Both the rolling and drawing processes introduces some amount of anisotropic properties, which is normally pronounced in aluminum, but less important in steels. Therefore, the material is taken as being isotropic and therefore, the tests in only one direction are sufficient. For that purpose, tensile tests were performed on dogbone specimens cut from the shell casing (see Fig. 1).

Now the empty casing was cut lengthwise and unrolled. Care was taken to unroll the empty casing which exhibited a great deal of springback. The final shape of the dogbone specimen was cut using a waterjet by placing the thin shell casing between two thicker plates of steel to keep it flat. Digital Image Correlation (DIC) was used to measure local strain. Load–displacement was measured using an MTS 200 kN Universal Test Machine with a 10 kN load cell. From the above true stress–strain curve (Fig. 1), the average flow stress of the shell casing was estimated to be $\sigma_o = 500$ MPa. This value is important in the analytical solution of

Table 1
Specifications of the 18650 cells.

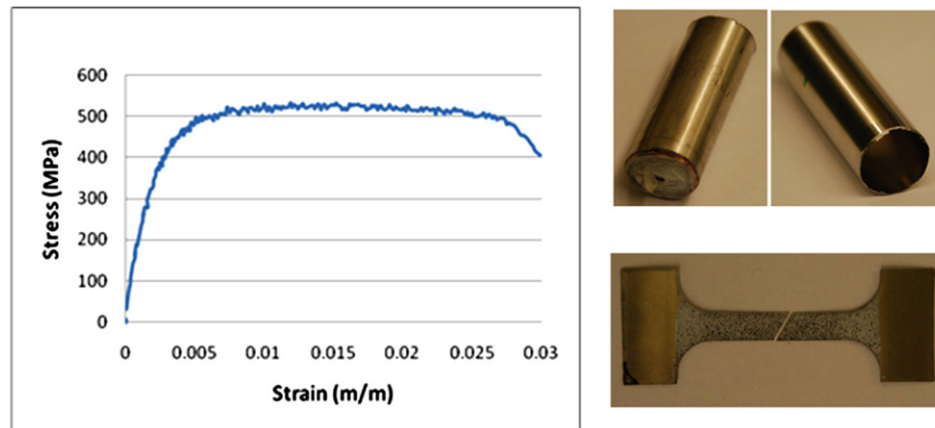|	
Nominal capacity	2600 mAh
Size	65 mm × 18 mm × 18 mm
Weight (Typical)	45 g
Charge method	Constant current and constant voltage (4.2 V)
Nominal voltage	3.7 V
Max. charge current	1CmA (2600 mA)
Max. discharge current	2CmA (5200 mA)
Discharge temperature	−20 °C–+60 °C
Energy density	565 Wh/l, 215 Wh kg^{-1}
Charging time	3 h (Standard) or 2.5 h (Rapid)

Fig. 1. 18650 shell casing (upper right), a fractured dogbone specimen from shell casing (lower right), and true stress–strain curve (left).

the shell casing which will be discussed in the Section 3. The determination of fracture strain would involve extensive uniaxial and biaxial tests, in conjunction with FE simulations of those tests. A detailed procedure has been described by one of the present authors (TW) in a number of publications [13,14]. The present uniaxial test provides only an estimation of the fracture strain, which is equal to $\epsilon_f = 0.03$.

2.2. Description of test equipment

The purpose of the test program is to get information on the global response of the cell as well as to detect the onset of short circuit due to mechanical loading. In order to accomplish this goal, not only the load–displacement relation of the punch was measured, but also the voltage output of the battery, as well as a possible temperature rise upon short circuit was recorded. Because the cylindrical cells are rated at 2600 mAh at full charge, the batteries were discharged as a safety precaution, to minimize the possibility of thermal runaway upon short-circuit. The test was conducted in an environmental chamber developed for this purpose. There were three separate output channels to measure: force–displacement, voltage, and temperature. Extraneous data recorded prior to the test element contact with the battery cell was deleted as well and the cross-head extension was set to zero at that point. Tests were stopped after a failure occurred .The descriptions of devices used for these tests are included below.

2.2.1. MTS loading frame

All tests were performed on the displacement control 200 kN machine equipped with a 10 kN load cell. The cross head speed is in the range of 0.1–1000 mm min^{-1} with deflection accuracy of 1%. A calibrated load cell with the capacity to measure up to 10 kN in compression was used for measuring the applied load in the tests. Each load cell has an accuracy level of 1% of the measured load. A flat steel block was used to hold the cylindrical compression test elements. The MTS software, Testworks 4, was configured for the attached load cell and a linear extension rate of 1.0 mm per minute was used during the tests. The system was also configured to automatically stop the test in the event of extension to the base plate, or if load exceeded the capacity of the attached load cell. The displacement of the cross head and measured force applied to the load cell was recorded versus time at a sampling rate of 1 Hz.

2.2.2. Voltmeter

A Radio Shack 46 Range Digital Multimeter was used to measure voltage of the batteries during the tests. The voltmeter is equipped with an RS-232 digital output and was connected to the MTS computer via a COM port. The meter has an accuracy of $+/-$ 0.3%

from 0 to 4 V. The supplied Meterview software was used to record the voltage output of the battery versus time. The software recorded the data at a rate of 1 Hz.

2.2.3. Thermometer

The Omega HH176 thermometer with a style II CO-2-K thermocouple was used to measure surface temperature of the batteries during the tests. The HH176 measurement device was connected to the MTS computer via a USB cable to record temperature readings. The HH176 has an accuracy level of $+/-$ 0.05% of the indicated reading. The thermocouple is constructed of proprietary Chromega–Alomega materials at 0.0005″ thick, has a response time of 2–5 ms and a maximum temperature of 540 C. The thermocouple was mounted on the underside of the battery to minimize interaction with the cooling effect of the ventilation box. The supplied software, Temp Monitor, recorded the temperature data versus time at a rate of 1 Hz. The temperature sensor was attached to the lateral surface of the cell.

2.3. Lateral indentation of the cell by a rigid rod

A cylindrical rod with radius of 8 mm was attached to the restraining block (see Fig. 2 right) and load was applied with a constant velocity of 1.0 mm min^{-1}. Fig. 2 (left) shows the measured force and displacement variation over time for the test performed on the 18650 cylindrical battery. The peak force and associated displacements for the test were 6469 N, and 6.3 mm, respectively. Fig. 2 (left) also shows the point of short circuit in the cell, as detected by a drop in force and voltage, as well as an increase in temperature. One can see from these figures that the peak force and drop in voltage occurs almost simultaneously, which confirms the occurrence of short circuit. The deformed battery is shown in Fig. 2 (right). The battery is tightly wrapped around the rigid rod.

Repeating an identical test reveals that there is a spread in the measured peak force; however, the magnitude of displacement at short-circuit is similar between the two tests, see Fig. 3.

2.4. Crush test by a hemispherical punch

In this test, the 18650 cell was crushed by a hemispherical punch of 12.7 mm diameter. Careful set up and measurement were used to make sure the center of the punch and cell were aligned, so that the cell will not slide under this loading scenario. The discharging procedure, and the details of instruments used to perform this test were similar to the previous test. The set-up of this test is shown in Fig. 4 (right). This test and the previous one would apply
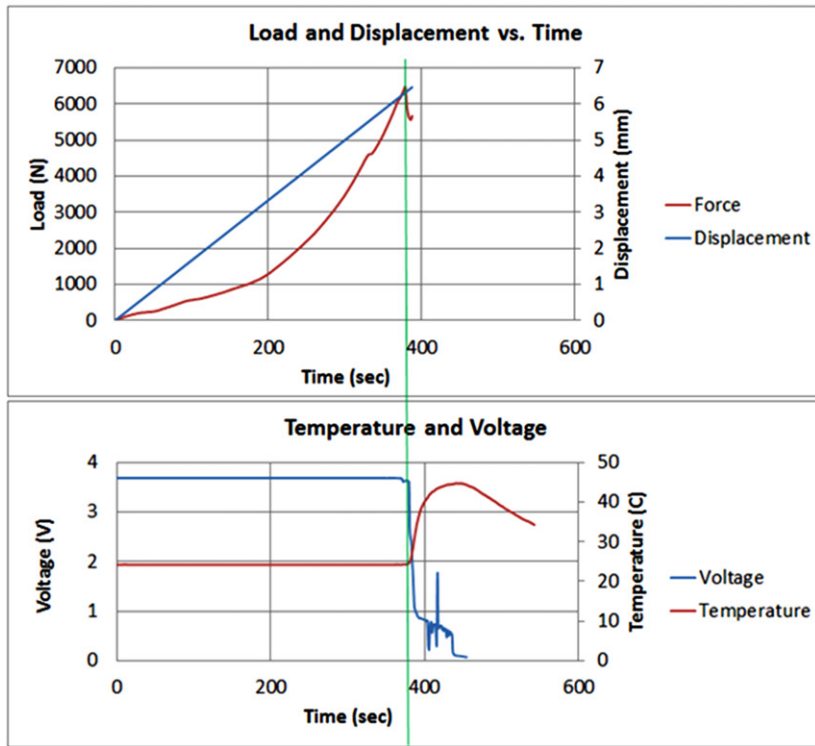
Fig. 2. Detecting the point of short circuit in rod indentation test from force, voltage, and temperature measurement (left), and deformed shape of the cell (right).

compressive stresses in the radial direction and tensile stresses in axial direction (in local coordinate system) under the punch. The difference between this test and the previous one is the tensile stresses could be applied both in axial and cross sectional elements, while in previous test, tensile stresses could only be developed in axial direction.

The variation of the force, displacement, voltage, and temperature versus time is shown in Fig. 4 (left). Again, it is seen that drop in the resisting force occurs at the same time as the drop in voltage. It is also observed that temperature starts to rise over a period of a minute and a half and falls back, which indicates release of the residual energy stored in the discharged cell. It will be shown in Section 4 that the short circuit occurs under the punch, which is far from the location of the temperature probe. The release of the heat around the point of short circuit should be much faster, and leading to larger temperatures. The present test could be of a value to research teams modeling thermal effects in abuse scenarios, see for

Fig. 3. Two identical tests, rigid-rod indentation.

example [15–17]. Fig. 5 shows repeating this test resulted in almost identical force–displacement curve.

2.5. Three-point bending test

In addition to indentation and crush tests performed to study point f short circuit of the 18650 cells, a three point-bending test was performed. The bending loading of cylindrical cells could actually occur as a result of a complex interaction of cells inside a module during a severe crash. The state of stress in the bending test is a combination of global stresses resulting from bending of a short beam, as well as local stresses under the punch. Fig. 6 shows the test set-up. The radius of the cylindrical indenter was 10 mm, and the radii of supporting cylinders were 24 mm.

All the measured parameters of the cell response are shown in Fig. 7. One can see that initially, there is a linear response suggesting that the cell (combination of shell casing and jelly-roll) is behaving in a linear elastic range. On the load–time diagram, three local peaks can be distinguished. The first peak corresponds to formation of small folds on the thin metal shell, causing a local drop in the force, and then the force level rises slightly, only to produce tensile fracture of the shell casing. It takes approximately another 1 mm of punch travel to initiate short circuit. Clearly, the jelly roll must have fractured internally. The precise location of the fracture zone could be determined by a CT-Scan.

An interesting observation from this test was the relatively low ductility of the shell casing. It was observed that before a short circuit in the jelly roll was detected, a crack developed in the tensile side of the shell casing, which resulted in leakage of electrolyte from the steel casing into the plastic wrap, see Fig. 8. Fracture of the shell casing initiated at $t = 350$ s, corresponding to punch displacement of 6.5 mm, see Fig. 7. The crack propagates quite far, almost two third of the diameter of the cell. The fracture of the shell casing must have accelerated the onset of electric short-circuit. This
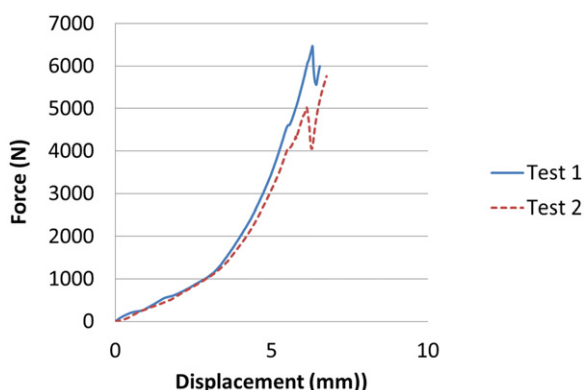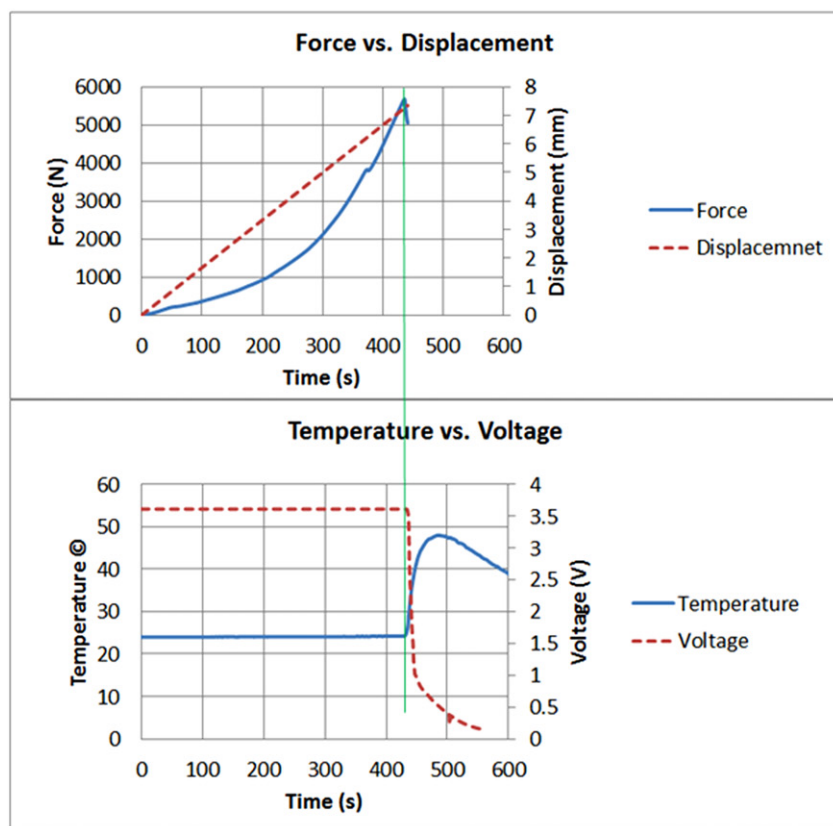
Fig. 4. Detecting the point of short circuit in hemispherical punch crush test from force, voltage, and temperature measurement (left), test set-up (right).

effect can be easily prevented at the design stage, by making the shell casing from a more ductile material, such as stainless steel.

Two apparently identical tests were run, and the comparison of load−displacement is shown in Fig. 9. One reason for the difference in the two tests could be due to difficulty in positioning the battery on two cylindrical supports. The strength of the cell along its axis is not symmetric, with higher crushing strength on the side with the cap assembly. Referring to Figs. 3 and 9, a spread in the experimental measured response of the cell indicates that it will not be possible to reach a perfect correlation with predictions of a model.

2.6. Compression of the cell (no endcaps) between two plates

In these series of tests the endcaps were removed, while the cylindrical shell casing was still present. This allowed full observation of the jelly roll during crushing and prevented the endcaps from acting as bulkheads resisting the crushing motion for which no easy analytical solution exists. Because of the absence of endcaps, it was not possible to measure the voltage output and therefore the onset of short circuit. This cell was fully discharged before testing. A sequence of the deformation mode of the cross-section of the cell is shown in Fig. 10. One can distinguish that there are individual windings. There is a flat region in the cross section of the cell, which is in contact with flat platens, and then there are two semi-circular regions connecting these flat sections.
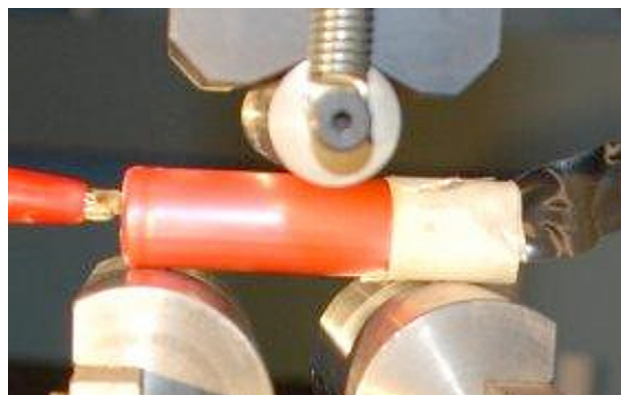

Fig. 5. Load−displacement for two identical tests, hemispherical punch indentation.

Fig. 6. Three-point bending test set-up.

Formation of folds in shell casing

Fracture of shell casing

Onset of short-circuit in the cell

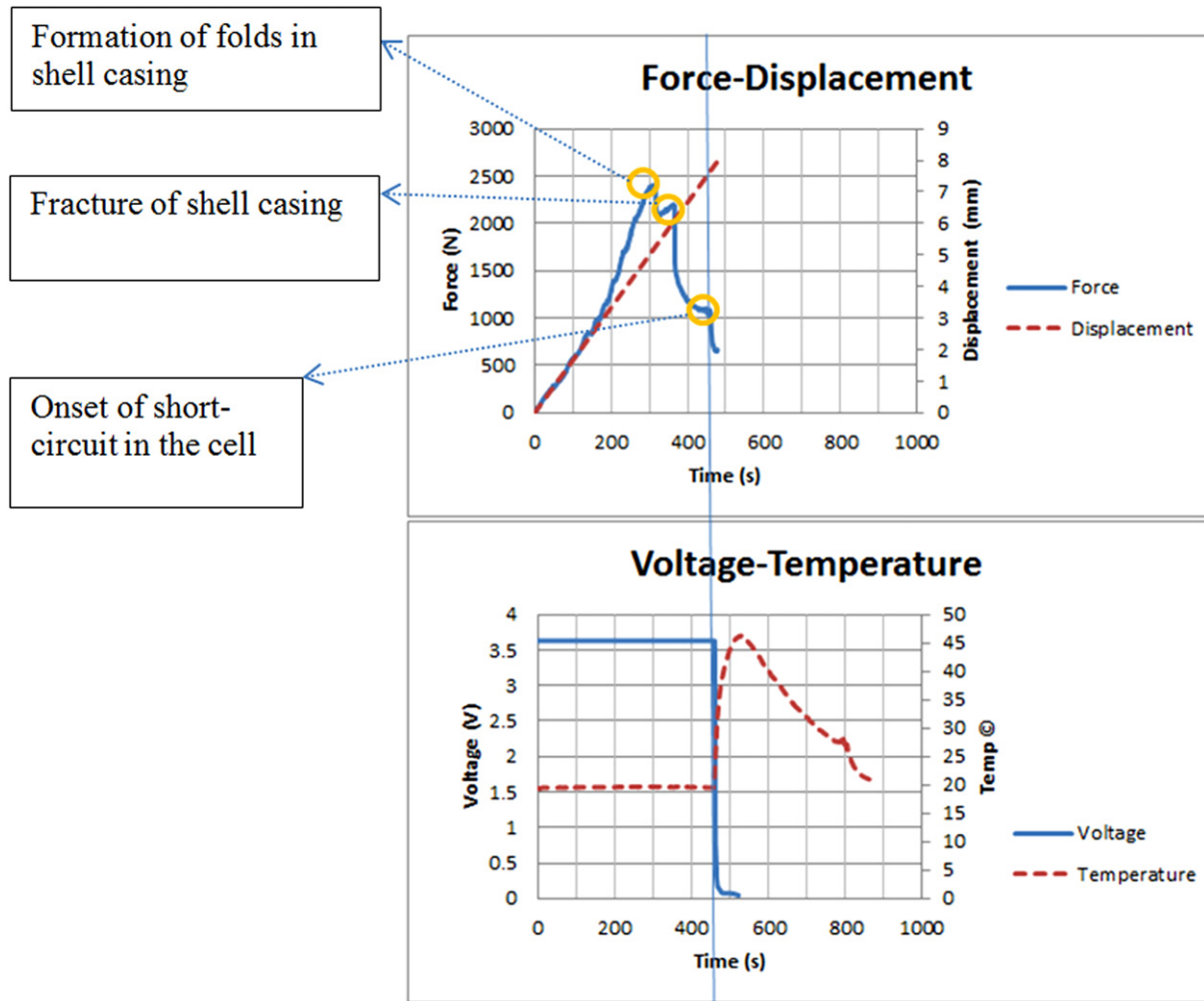**Force-Displacement**

Voltage-Temperature

Fig. 7. Force, displacement, voltage, and temperature measurements during 3-point bending test.

The small diameter center metal tube is progressively crushed and completely disappears halfway through. The most important experimental observation is the delamination of the layers of jelly roll in the region inside the two semi-circular portions of the deforming cell. This phenomenon indicates for a need to consider an anisotropic model for the cell. This issue will be further explained in the Section 6, Discussion.

Two tests were performed. The measured load–displacement curve is shown in Fig. 11 (left). It is seen that up to 7 mm crush distance the results were almost identical. There is a drop in force in

Test 2 at about 30,000 N and 6 mm of deformation, while in Test 1 force increased up to 40,000 N. The drop of the force is associated with the ejection of the jelly roll out of the shell, clearly seen in Fig. 11 (right). The process of ejection depends very much on friction, which in turn depends on the amount of electrolyte
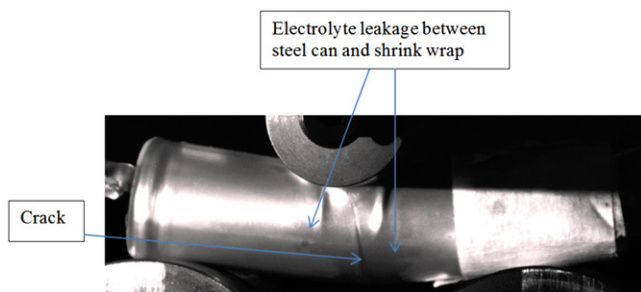
Electrolyte leakage between steel can and shrink wrap

Crack

Fig. 8. Development of crack and leaking of electrolyte in the lower side of the cell under tensile loading.
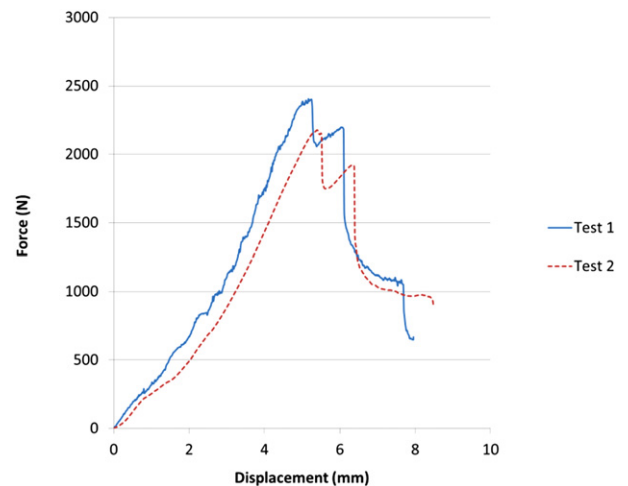
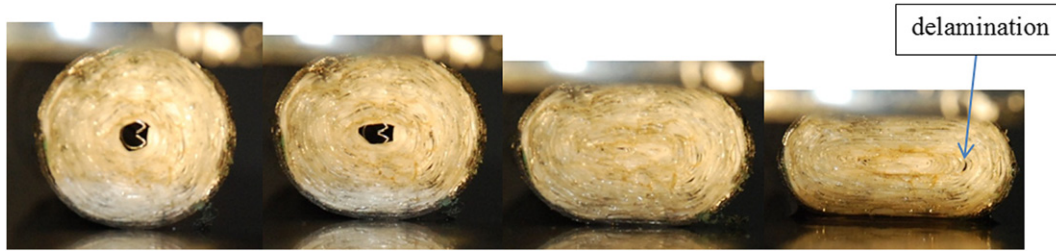**Fig. 9.** Load–displacement curve for two identical tests, 3-point bending.

Fig. 10. Sequence of crushing during the lateral crush test.

evaporated during the test. Observations from this test provide very important clues for the development of an improved constitutive model of the jelly-roll [18].

3. Estimation of strength of shell casing

The crushing strength of a cell comes from both the strength of the outer shell casing and the crush-resistance of the interior core winding. The analysis of the empty shell will provide a quick estimate about the contribution of the shell casing to the overall strength of the entire cell. Closed form solutions of a thin cylindrical shell with and without endcaps exist in the literature and will be reviewed under two types of loading: lateral indentation by a rigid rod and lateral compression between two plates.

The static and dynamic response of a thin pipe subjected to a rigid punch loading was studied in a series of publications by one of the present co-authors [19,20]. The solution that would be most useful to the present problem refers to the resistance of the free end cylinder subjected to lateral knife type of loading. The relationship between the indentation force F and the indentation depth δ is given by:

$$F_{\text{shell}} = \sigma_0 t^{1.5} \sqrt{2\pi\delta} \tag{1}$$

where σ_0 is the average flow stress of the material of the shell casing, which was determined in the previous section, and t is the thickness of the shell. The above equation is valid in the range of the punch travel not greater than the radius of the shell. It should be noted that the radius of the cylinder does not enter in Equation (1). The accuracy of the above solution was shown in the literature to compare well with full scale and component tests of pipes subjected to wedge type of loading. Considering this solution, the contribution of shell casing of the 18650 cell to the total force in a rigid rod indentation scenario is less than one percent (0.25 kN),

as compared to the force generated by the local indentation of a cell by a cylindrical rod (see Fig. 2).

The second problem of interest to this study is lateral crushing of an empty tube with endcaps removed between two rigid plates. We adopt here a very realistic closed form solution of this problem derived by Runtz and Hodge [21]. The crushing force is related to the crush distance through the following equation:

$$F_{\text{yshell}} = \sigma_0 t^2 \left(\frac{L}{R}\right) \frac{1}{\sqrt{\left(1 - \left(\frac{\delta}{R}\right)^2\right)}} \tag{2}$$

where L and R are the length and radius of the battery, respectively. Considering the above simple closed form solution, the shell casing accounts again for less than one percent (0.1 kN) of the resistance of the cell when compressed between two flat plates. It can be concluded that the force generated by the empty outside casing is more than two orders of magnitude smaller than the total resistance of the cell under these two loading condition. At the same time, it is noted that the outside casing is important for containing the jelly roll in its designated shape, which will be the case for three-point bending. In the latter case, the shell casing can contribute up to half of the bending strength of the cell [22].

3.1. Constitutive model of the jelly roll

In the case of pouch batteries, the lateral compression of the cell between rigid blocks results in a uniform state of stress and strain. Therefore, it is relatively simple to drive the stress–strain curve from the load–displacement curve. For the cylindrical cells, the stress and strain states are highly non-uniform and change during the loading process. In this paper a homogenized model of the jelly roll is adopted, in which the contribution of all components of the interior layered structure of the battery is lumped together into
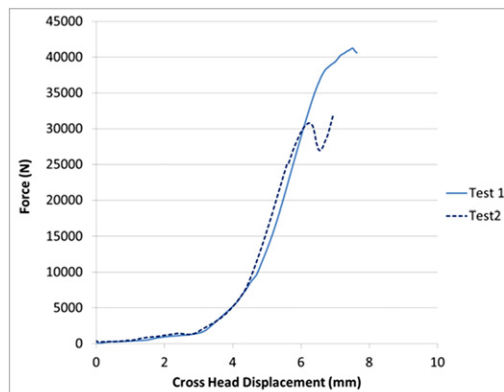

Fig. 11. Measured load–displacement curve for two identical tests, and a picture of the deformed cell.

a single type of material. In other words, in this model the contribution of individual components of the jelly roll is not quantified. At the same time, it is recognized that compressive and tensile properties of this material are different. From previous modeling of lithium-ion cells, it is understood that the jelly roll material behaves like compressible foam until densification [10]. The stress–strain curve obtained for pouch cells in compression is shown in Fig. 12. A simple fit of that measured curve is a parabola:

$$\sigma = B\epsilon^2 \qquad (3)$$

where $B = 550$ MPa. It should be noted that the active material in pouch batteries tested earlier in our lab and in the present cylindrical cells are both $LiCoO_2$ (cathode)/graphite (anode). Considering that about 80% of the volume of the cell is filled by active material, it is assumed that stress–strain curve determined for pouch batteries could also be used for the present cylindrical cells. The validity of this assumption will be checked by comparing results of simulations with such material input to the four experiments described in Section 2. In the numerical simulation, either an analytical fit, Equation (3) or the actual measured curve could be introduced.

In tension, there is a complicated process of failure which could be captured by introducing a cut-off value for the tensile strength. This value controls the onset of short-circuit. In the present paper, the magnitude of tensile cut-off was calibrated from the rigid-rod indentation test, and then validated against the hemispherical punch test. The value of tensile cut off was determined to be $\sigma_{TC} = 10$ MPa. According to the present model, when the tensile stress in a representative volume element reaches the cut-off value, it is held constant for the rest of the simulation, see Fig. 12.

4. Finite element modeling

A finite element model of the cell was developed in LS Dyna software. The shell casing of the cell was discretized using 4-node fully integrated shell elements. The jelly roll was modeled by fully integrated solid elements. The rigid rod/punch and rigid plates were modeled using contact entity from LS Dyna contacts, which assumes a rigid geometrical shape for the contact surface. There were 11,167 shell elements and 29,106 solid elements in the model. The size of the shell and solid elements were approximately the same (0.8 mm). Material piecewise linear plasticity from library of LS Dyna materials was used for the shell casing. The following input was used for the steel shell casing: $E = 200$ GPa, $\nu = 0.3$, and $\sigma_{yield} = 450$ MPa. The effective stress versus effective plastic strain curve was input to the model from the dogbone specimen test. The combined shell and solid model is shown in Fig. 13.
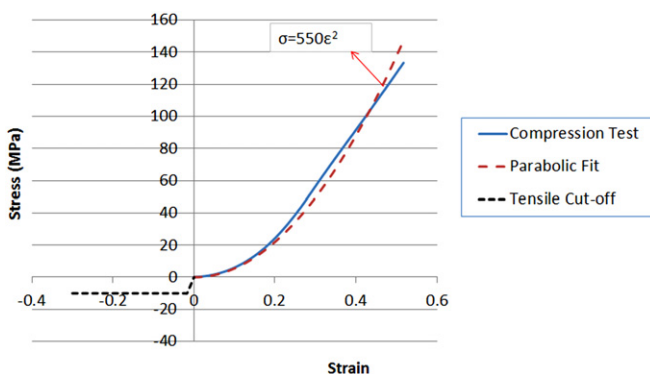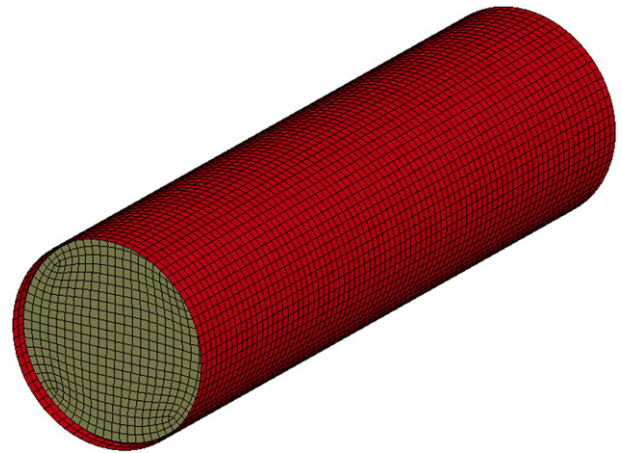

Fig. 13. Finite element model of the jelly roll and shell casing.

For the jelly roll, the material crushable foam from the library of LS Dyna was used. The stress–strain curve, shown in Fig. 12 was used as the input to all finite element simulations. The rational for choosing this model is that it is consistent with our experimental observation. First, the stress–strain curve obtained from compression test on pouch batteries exhibits a concave shape, which is characteristic for compressible foam with a very low plateau stress. Secondly, this foam model admits different properties in tension and compression. Specifically, the response in tension is elastic with limit on tensile strength, which is referred to as a "cut-off" value. The cut-off stress is determined by inverse method, by performing simulation to match the onset of failure in the rigid-rod indentation test, $\sigma_f = 10$ MPa. The Young modulus could be either introduced as an input number or will be calculated from the stress–strain curve in compression. The maximum slope of the input compression curve is then compared with the value introduced as an independent input, and the largest of two is taken. For present model, the Young modulus was 500 MPa. Using 8 CPUs to run the simulation, the indentation simulation took approximately $2\frac{1}{2}$ h, for a relatively small mesh size (0.8 mm in length).

5. Validation of the model

Four loading scenarios were simulated to validate the material model by comparing the experimentally measured and simulated load–displacement curve. This includes indentation by a rigid rod, hemispherical punch crush, three-point bending, and compression between two flat plates.

5.1. Indentation by a rigid rod

Fig. 14 shows the comparison of rigid rod indentation simulation with the test. It can be observed that the model was able to predict the load–displacement relationship of the cell through the indentation with very good accuracy. The model also detects the onset of short circuit by the point of a local drop in the force. The point of short circuit in the test occurred at a force level of 6469 N and displacement of 6.3 mm. In the simulation, the peak force is 6532 N at 6.6 mm of deformation. It was observed in experiments that voltage and temperature measurements also verify a short circuit at this point.

Location of failure (assumes short-circuit) is detected as the first point reaching and maintaining a principal tensile stress of 10 MPa, see Fig. 15. The short-circuit was found to be in the intersection of
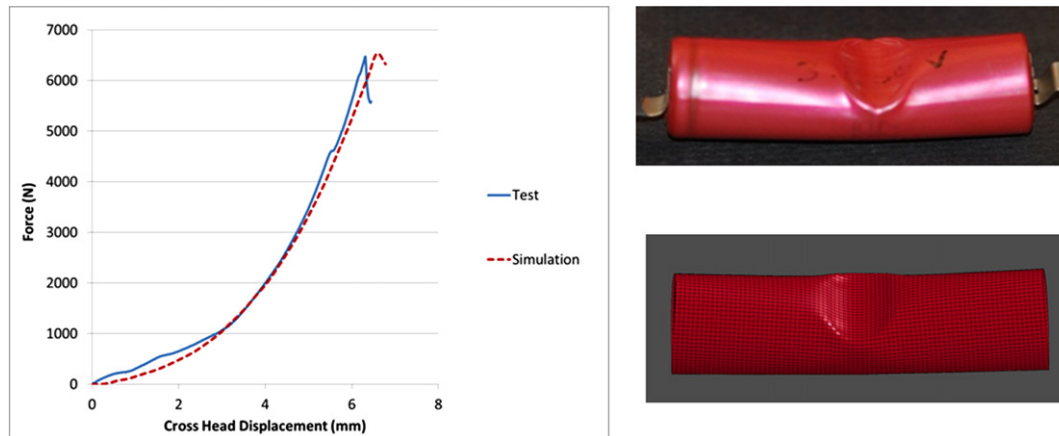

Fig. 12. Experimental stress–strain curve, from uniaxial compression of pouch cells with similar chemistry.

Fig. 14. Rigid rod indentation test versus simulation.

two planes of symmetry of the cell, at the depth of 4 mm under the punch.

5.2. Hemispherical punch crush

Fig. 16 shows the simulation of hemispherical punch crush. Again, it can be observed that the model closely follows the experimental force–displacement of the cell. The model also detects the onset of short circuit, which is evident from a drop in force. The measured peak force was 5681 N at 7.3 mm. The respective values predicted from the simulation were 5647 N and 6.9 mm. It should be noted that the agreement between theory and simulation for the rigid rod indentation was perfect, while in the case of spherical punch indentation, the calculated curve is slightly higher than the experimental one. This was to be expected from the model, in which the difference of anisotropic properties in the axial and hoop direction is not accounted for. Still, the error in predicted peak force is less than 1%.

Location of short circuit is detected as the first point reaching and maintaining a tensile principal stress of 10 MPa, see Fig. 17. As before, failure (short-circuit) occurs at a location under the punch with identical depth (4 mm) as rigid rod indentation test.

5.3. Three point bending simulation

In the two previous loading cases of a cylindrical and hemispherical punch, the cell response was mainly controlled by the compressive stress–strain relation and the magnitude of the tensile cut-off stress. The bending problem of the cell introduces very complex and inhomogeneous state of stress inside the jelly roll and the shell casing. There are many more parameters influencing the overall bending response as well as local fracture response, which are listed below. In order to get a full understanding of the deformation and failure process, a thorough parametric study of the influence of all of the above parameters should be performed. In this paper only limited study was made, by taking fixed values of

some of the parameters and varying the remaining parameters. The assumed computational model is briefly described below.

Taking only three values of each of the above parameters would result in $3^{10} = 59,049$ simulations, which is unmanageable. Therefore only a partial parametric study was performed by keeping the first four parameters in Table 2 fixed and taking limit values (upper and lower bounds) on the remaining parameters. The global properties of the cell, such as load–displacement relation and energy dissipated are not strongly sensitive to specific values of the input parameters. At the same time local properties such as onsets of buckling and fracture of the shell are highly dependent on the values of many parameters.

The simulation predicts well the initial portion of the load–displacement curve, the peak value of the load, and the subsequent drop in the force. The agreement between the measured and calculated absorbed energy is within 1% error. At the same time, the point of initial buckling of the shell casing on the compressive side, which triggers the subsequent tensile fracture, is predicted slightly lower than the test value, see Fig. 18.

The onset of buckling is controlled to a larger extent by the thickness of the shell casing. The effect of thickness of shell casing on the load–displacement curve was studied and is shown in Fig. 19. The steel and aluminum shell casings are typically made by process of deep drawing of sheets, leading to a non-uniform distribution of wall thickness along the longitudinal axis of was cylinder. For the present cell, there is a considerable thickness variation from 0.32 mm at the bottom cap to 0.18 mm on the edge of the top cap assembly. This explains the range of thickness chosen for this study. The point of buckling occurs under the punch in the middle section of the cell. The corresponding thickness is estimated to be halfway between the measured values, which is 1/2(0.32 + 0.18) = 25 mm. Indeed, the simulated curve corresponding to 0.26 mm was the closest to the measured one; this value was used for the simulation shown in Fig. 18.

In general, the material ductility measured by the equivalent strain to fracture depends on the stress triaxiality. The finite element
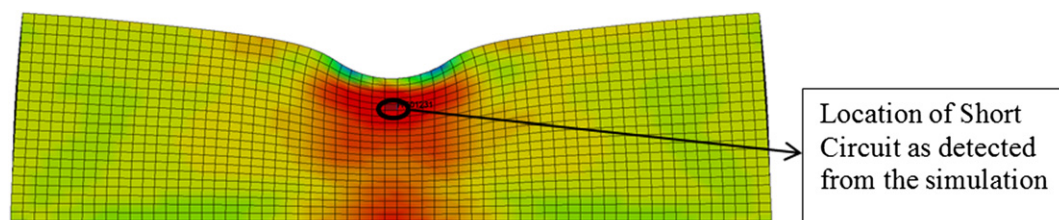

Fig. 15. Location of short circuit, contour of 1st principal stress, rigid rod indentation.
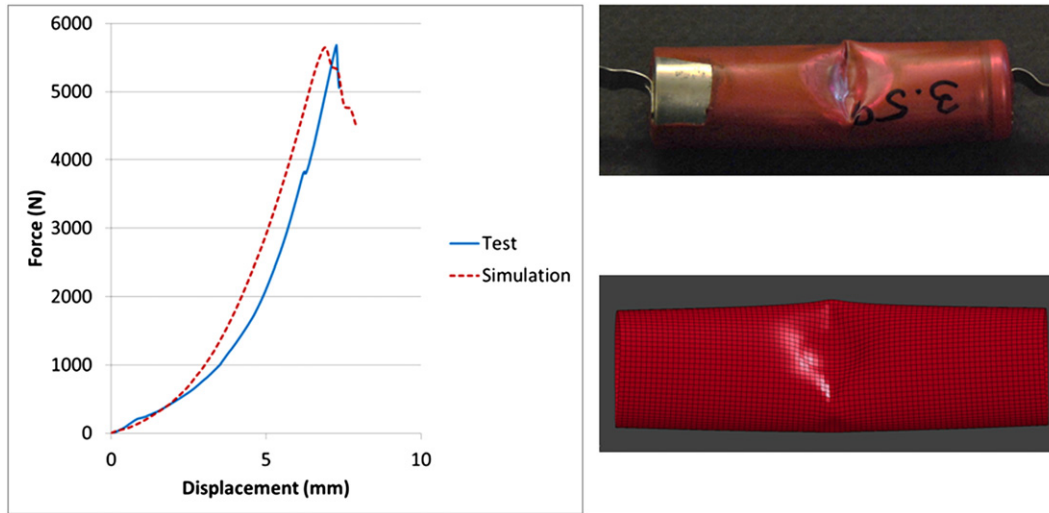
Fig. 16. Comparison of tests and simulation for the hemispherical punch crush loading.

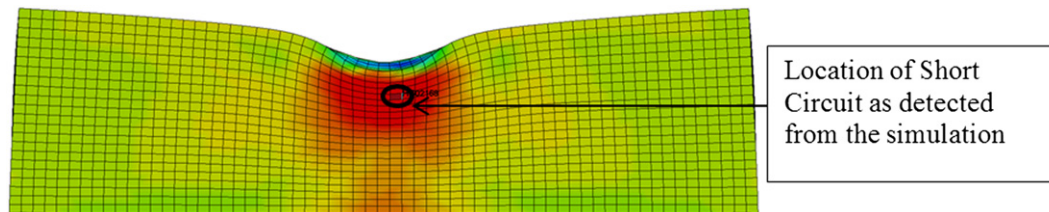Location of Short Circuit as detected from the simulation

Fig. 17. Contour of 1st principal stress, hemispherical punch crush, a CT scan of the damaged cell is being performed to verify the location of short circuit.

simulation revealed a very interesting interaction between the deformation process in the jelly roll and stresses and strains in the shell casing, which will help in simplifying the fracture model. For thin shells, the fracture should initiate under transverse plane strain condition for which the stress triaxiality is equal to $1/\sqrt{3}$. However, when plotting the calculated stress triaxiality at the element where first fracture occurred, the value of stress triaxiality was initially close to 2/3. When looking into individual components of the stress tensor, the maximum tensile stress in the length direction was about 600 MPa, while the maximum hoop stress for the same shell

Table 2
Parameters affecting the response of the cell in 3-point bending test.

Parameter	Range of values
Compressive strength of the jelly roll in terms of the stress–strain input curve (in the simulation the actual measured curve was inputted)	$\sigma = 550\epsilon^2$
Plastic properties of the shell casing defined by the stress–strain curve	$\sigma = 1074\epsilon^{0.16}$
Young modulus of the jelly roll in tension	$E = 500$ MPa
Cut-off value for the tensile stress of the jelly roll	$\sigma_{TC} = 10$ MPa
Mesh size of the shell discretization (this influence formation of local folds)	0.2×0.8–0.8×0.8 mm
Coefficient of friction between cell and supports	$\mu = 0.1$–0.3
Distance between supports	$l = 58$–60 mm
Shrink wrap representation	Lumped into an equivalent thickness with shell casing
Equivalent thickness of shell casing	Thickness = 0.18–0.3 mm
Fracture properties of shell casing	$\epsilon_f = 0.03$–0.05

element was approximately 350 MPa. The only mechanism for generating such a hoop stress was a large local pressure exerted by the jelly roll on the outer shell. To explain this interesting interaction, the history of stress components in the solid element adjacent to the shell element was reviewed. It was found that the largest (radial) compressive stress was 8 MPa. In the theory of membrane shells, the hoop stress, σ_θ, is related to the normal pressure, p, by:

$$\sigma_\theta = \frac{pR}{t} \tag{4}$$

where R and t are respectively radius and thickness of the shell.

For the geometry of the present cylindrical shell, this gives the value of the hoop stress 340 MPa, very close to the value retrieved from the FE simulation. It can be concluded that the pressure under the cylindrical punch is responsible for changing the stress state on the shell casing of the cell. Thinking of the cylinder as a short beam subjected to 3-point bending, one would expect the dominant stress to be the axial stress resulting in plane strain condition. In reality, the stress is closer to equi-biaxial tension. It was found through numerical simulation that the stress state close to the equi-biaxial tension precedes for all elements on the path of the advancing crack. It is therefore possible to use a simple fracture model with a constant value of equivalent strain to fracture. Because the ductility in equi-biaxial tension is often larger than in plane strain, the magnitude of the fracture strain was increased from the measured value of 0.03–0.04. The remaining parameters in this simulation were $l = 60$ mm, and $\mu = 0.3$. Fig. 20 shows a comparison of shape of the deformed cell in the test and simulation.

As explained in previous load scenarios, short circuit was detected at the element that reaches and maintains a tensile stress of 10 MPa. Point of short circuit in this simulation was detected in a cross section at the middle of the cell and at tensile side of the beam as shown in Fig. 21.
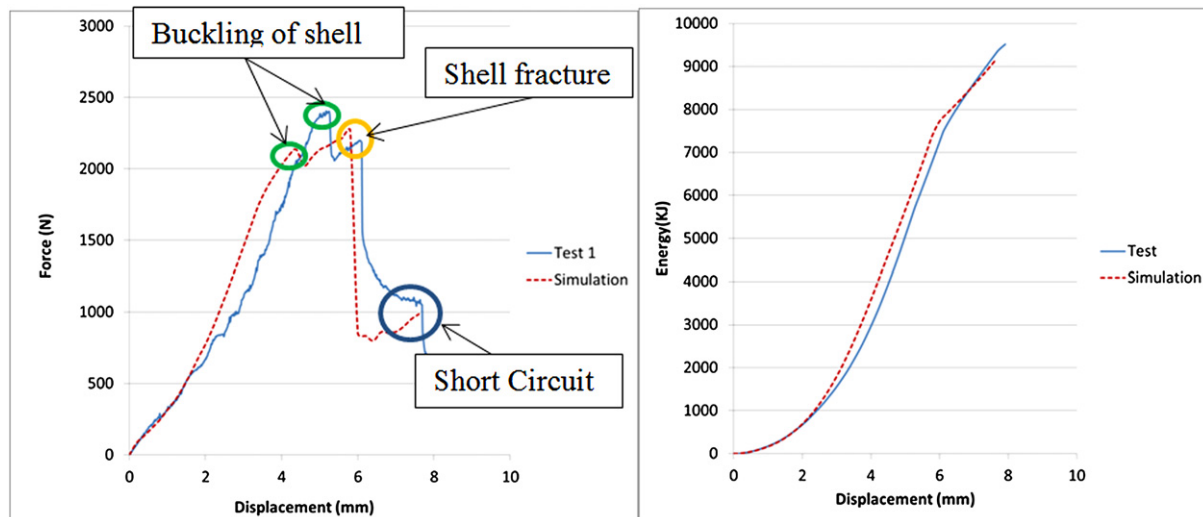
Fig. 18. Force−displacement (left), and absorbed energy (right) in 3-point bending test and simulation.

5.4. Compression between two flat plates

The simulation of this loading scenario initially over predicts the level of the force, but later on catches up with the experimental trend. What is significant here is that the model predicts the local peak due to ejection of the jelly-roll out of the shell casing at 6 mm displacement and 31,000 N as shown in Fig. 22. In the next section, the significance of this test for the development of a more exact constitution law will be discussed.

6. Discussion and future work

6.1. Delamination

The computational model of a cylindrical battery developed in this paper correctly predicts the response of a single cell for three different abuse scenarios. The material model is isotropic so that strength in all three directions is the same. This means that strength in radial and hoop direction is the same both in tension and compression quadrants. This hypothesis works well for the three loading cases, but over predicts the cell resistance in the compression test between two rigid plates. This discrepancy is well understood and it is caused by the process of progressive

delamination in the radial direction along the horizontal plane of the cell. This could clearly be seen from the photograph of the picture of the partially crushed cell, as well as FE simulation of a new model of the layered structure, see Fig. 23. The layered model is now at the stage of validation and will be described in an upcoming publication [18]. In the present homogenized computational model, a part of the strength is coming from the direction in which delamination occurs. Consequently, the compressive strength of the battery is predicted to be higher than the measured value, refer to Fig. 22.

6.2. Anisotropy

It is recognized that several simplifying assumptions were made in the derivation of the model. The laminated system of the core is responsible for structural anisotropy, and the amount of anisotropy should carefully be evaluated. Four constituent components of the jelly roll (anode/cathode particles and current collectors) are approximately isotropic. The separator has a significant in-plane anisotropy, but its relative contribution to the strength of jelly-roll is small. The aluminum and copper foil are very thin and also are
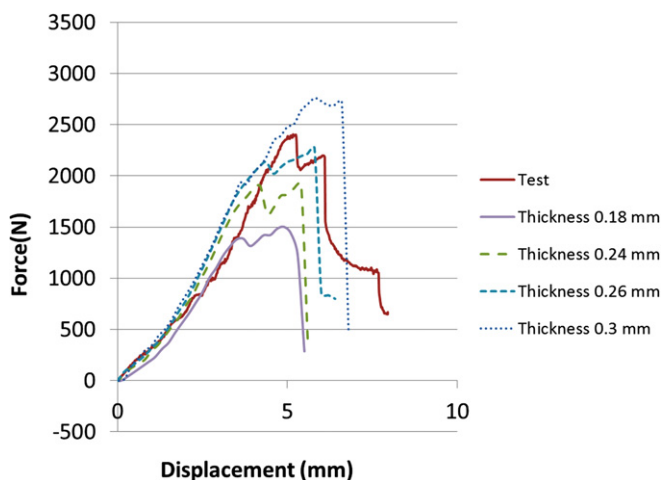

Fig. 19. Comparison of the load−displacement curve for several values of shell thickness with test results.
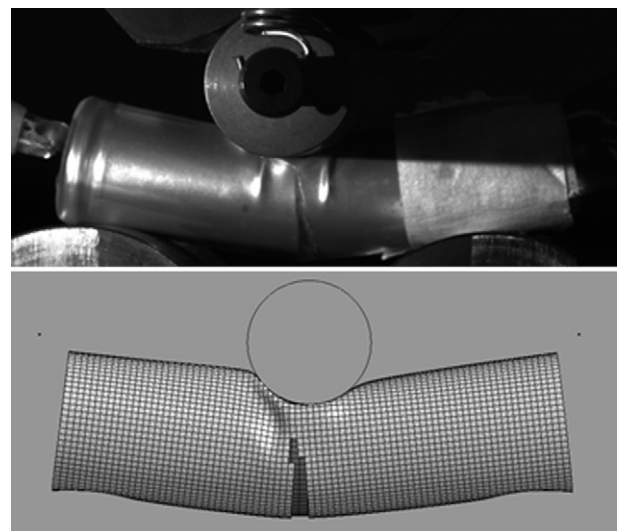

Fig. 20. Shape of the deformed cell and fracture line in test (up) and simulation (down).
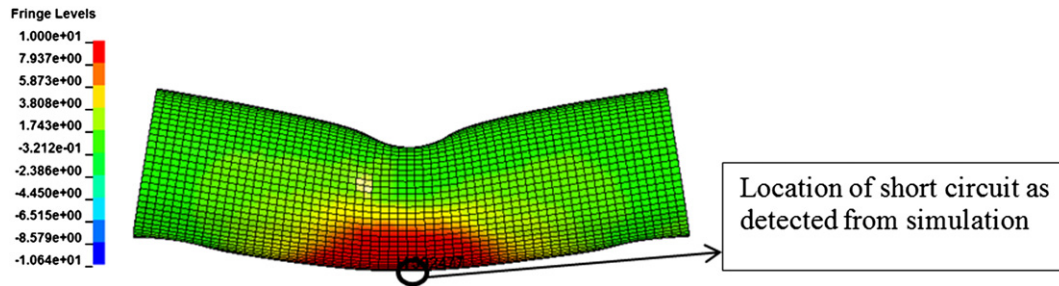
Fig. 21. Contour of 1st principal stress, 3-point bending simulation.

practically incompressible compared to the active particle coatings. The porous microstructure of coating/electrolyte allows for substantial compressibility, and this part of the electrode assembly may be the controlling factor of the constitutive model for the whole system. The active particle coatings are assumed to be an isotropic medium. The volume fraction of the active particles is almost an order of magnitude larger than the volume of the electrode/separator assembly. This feature alone is not sufficient to make the entire system to behave in an isotropic manner. It is believed that the layered nature of the system is responsible for a structural anisotropy. Therefore, the layout of the multi material system of aluminum foil and copper foil and polymeric separator calls for the development of a new type of the representative volume element. Such a model will be developed as a continuation of this research.

6.3. Relative merits of pouch versus cylindrical cells

A question often asked by the industry is which form factor is better, prismatic or cylindrical. Of course, the issue has many facets, including thermo mechanical properties, power versus energy, packaging, and resistance to mechanical abuse. From the point of view of mechanical response, there is a way to compare the performance of two types of cells. One measure of such a comparison is to calculate/measure the amounts of energy absorbed by the cells up to the onset of short-circuit. In a previous publication [10], the present investigation team studied the deformation and failure of small pouch batteries and found the strengths and determined the load–displacement under the punch indentation. The response of the two types of the batteries can now be compared under identical loading conditions, see Fig. 24. The difference between cylindrical and prismatic batteries clearly comes from a different form factor. The two cells tested in our program had similar

chemistry (LiCoO$_2$/graphite), but no statement can be made about the type of separator. Cylindrical batteries are wound and each layer provides considerable resistance in the hoop direction to underlying layers. At the same time the prismatic/pouch batteries are stacked and form a laminated plate with subsequent layers not transmitting any tension or shear. Therefore they are more susceptible to delamination and buckling. The different capacity for local energy absorption can be clearly seen in Fig. 24. The interested reader can further investigate the relative benefit of these two form factors on his/her own. In this paper, only the basis for such comparison was formulated.

6.4. Electric short-circuit versus battery thermal runaway

For the benefit of the readers, we would like to clarify that the onset of electric short-circuit is a necessary, but not sufficient condition for the occurrence of thermal runaway in the case of mechanical abuse. In reality, internal short circuit happens due to the failure of separator under tensile loads. The sequence of failure could be predicted using a detailed model of the layered structure of the jelly-roll, which is under development [18]. In the present paper, a procedure was presented to predict onset of electric short circuit using a homogenized model. In this level of modeling, the properties of all layers are lumped together into a single material model. Failure in tension occurs at a stress equal to cut-off value. The success of our predicting the force–displacement comes from the fact that volume-wise, active particle coatings are the largest fraction of the jelly-roll. It is believed that the failure of a separator occurs instantly when adjacent layers fail, and all the force that those layers were bearing transfers to the separator.

The fact that a battery gets an internal short-circuit does not mean that it will go to thermal runaway. The latter depends on
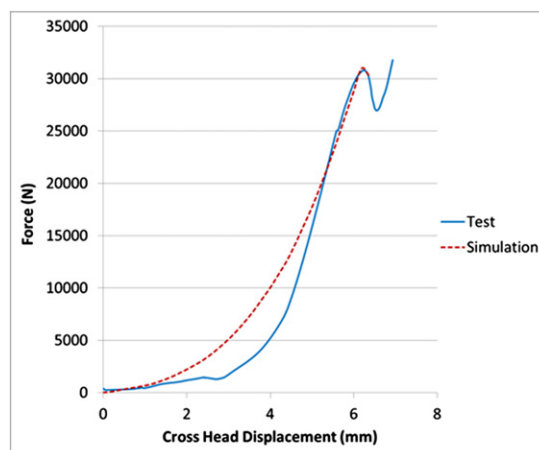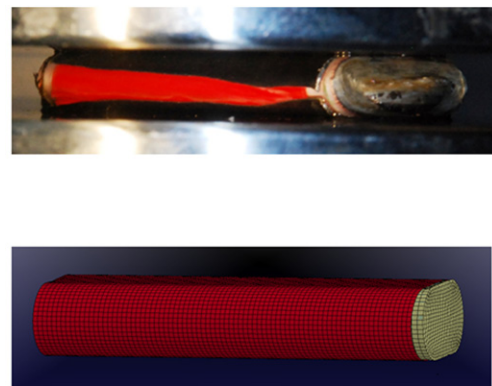

Fig. 22. Comparison of tests and simulation for the compression between two flat plates without endcap. The local peak in Test 2 and in the simulation shows the point were jelly-roll was squeezed.
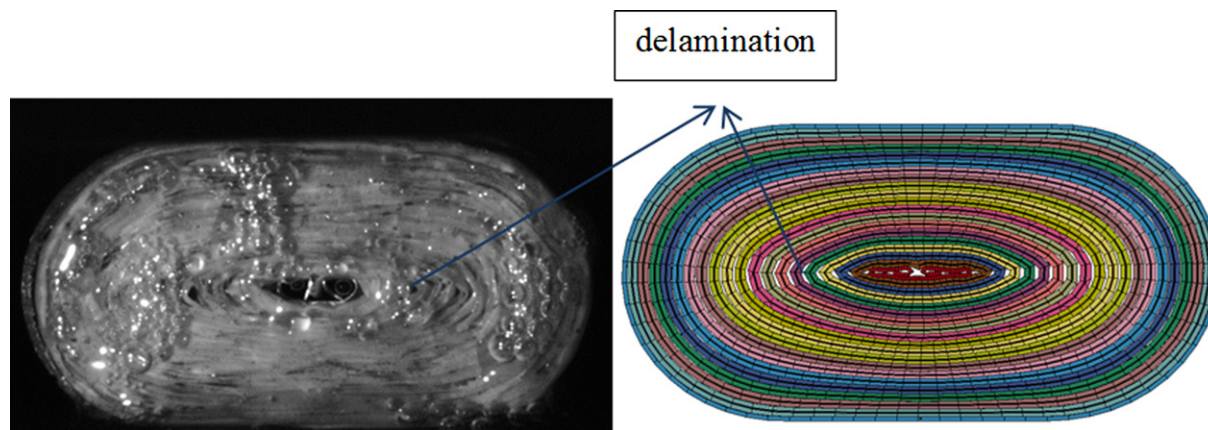
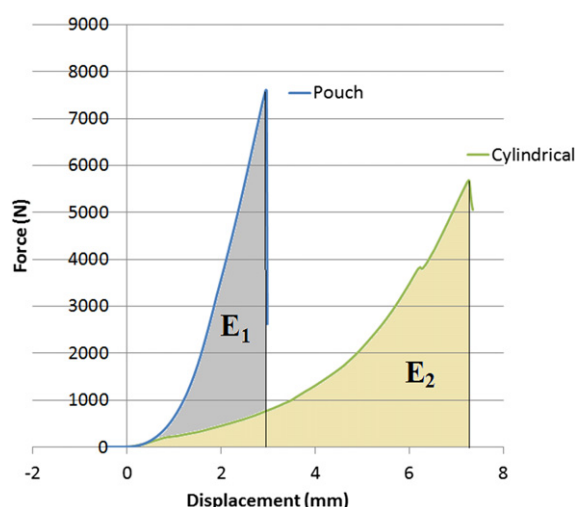**Fig. 23.** Delamination of layers during compression between two flat plates.

Fig. 24. Indentation of a hemispherical punch of 12.7 mm into small pouch and 18650 cylindrical cells with LiCoO$_2$/graphite chemistry. Area S1 and S2 represent the amount of energy absorbed up to the onset of short circuit.

many factors, such as chemistry of the cell, resistance of separator to heat, size of the fractured part, rate of heat transfer, etc. If the cell has not gone to thermal runaway right away, it can still go into a slow process of electrochemical reaction, releasing gases that eventually could lead to a catastrophic event. Also, a dead cell inside a battery pack can distort the electric balance of the pack and end up in uncontrolled consequences. Therefore, the authors believe that it is very important to detect onset of electric short-circuit even if this does not mean instant thermal runaway.

7. Conclusion

A comprehensive set of tests were performed on commercially available 18650 cylindrical cells. The cells were tested in about 10% SOC. The voltage was measured and onset of short circuit was detected. Temperature was also measured at a surface point of the cell. Four different loading configurations were considered, including lateral indentation by a rigid rod, indentation by a hemispherical punch, 3-point bending, and compression between two rigid flat plates. Outputs from the tests were force, displacement, voltage, and temperature versus time. A homogenized and isotropic computational model was developed that captures the global response of the cell under four different loading conditions. In addition, local failure of the jelly roll under the punch predicted with good accuracy the onset of short circuit in two loading

scenarios. The local failure in the test was detected by local peak in the resisting force, and simultaneous drop in voltage indicating onset of short circuit. This was further reinforced by the observed rise in temperature following failure. In the computational model, the short circuit is predicted as the point of local peak in the force, and the location of short circuit is assumed to occur at the first element with a tensile principal stress of 10 MPa. A very good correlation with the test was obtained for the two loading cases where compression was a predominant stress state under the punch. The limitations of the model were discussed and they were attributed to inadequate description of response of the representative volume element in dominantly tensile loading, as in the 3-point bending scenario. It is concluded that a model of crushable foam provides a good approximation to the behavior of the jelly roll under predominantly compressive loads.

References

[1] B. Smith, DOT HS 811 573 (2012).
[2] C. Ashtiani, AABC-09 Conference, 2009.
[3] J. Nguyen, C. Taylor, INTELEC 2004, IEEE, 2004, pp. 146—148.
[4] M. Otsuki, T. Ogino, K. Amine, ECS Trans. 1 (2006) 13—19.
[5] G. Henriksen, D. Vissers, A. Chilenskas, J. Power Sources 54 (1995) 134—137.
[6] P. Balakrishnan, R. Ramesh, T. Prem Kumar, J. Power Sources 155 (2006) 401—414.
[7] Y.H. Chen, C.W. Wang, X. Zhang, W. Shyy, A.M. Sastry, (2006).
[8] S. Golmon, K. Maute, M.L. Dunn, Comput. Struct. 87 (2009) 1567—1579.
[9] X. Zhang, A.M. Sastry, W. Shyy, J. Electrochem. Soc. 155 (2008) A542.
[10] E. Sahraei, R. Hill, T. Wierzbicki, J. Power Sources 201 (2012) 307—321.
[11] E. Sahraei, T. Wierzbicki, R. Hill, M. Luo, SAE Technical Paper (2010) pp. 01—1078.
[12] Sahraei E., Hill R., Wierzbicki T., Proceedings of the Battery Congress, 2011.
[13] Y. Bai, X. Teng, T. Wierzbicki, J. Eng. Mater. Technol. 131 (2009) 021002.
[14] Y. Bai, T. Wierzbicki, Int. J. Mech. Sci. 50 (2008) 1012—1022.
[15] R.M. Spotnitz, J. Weaver, G. Yeduvaka, D. Doughty, E. Roth, J. Power Sources 163 (2007) 1080—1086.
[16] R. Spotnitz, J. Franklin, J. Power Sources 113 (2003) 81—100.
[17] S. Santhanagopalan, P. Ramadass, J.Z. Zhang, J.Power Sources 194 (2009) 550—557.
[18] E. Sahraei, T. Wierzbicki, in preparation.
[19] T. Wierzbicki, M. Suh, Int. J. Mech. Sci. 30 (1988) 229—248.
[20] M.S. Hoo Fatt, T. Wierzbicki, Int. J. Mech. Sci. 33 (1991) 999—1016.
[21] J.A. DeRuntz Jr., P.G. Hodge Jr., J. Appl. Mech. 30 (1963) 391.
[22] S. Santosa, J. Banhart, T. Wierzbicki, Acta Mech. 148 (2001) 199—213.